Modeling, Design, and Evaluation of a Parallel Robot for Cochlear Implant Surgery

Jason Pile, *Student Member, IEEE*, and Nabil Simaan, *Member, IEEE*

Abstract—Cochlear implant surgery is a procedure that requires delicate insertion of an electrode array into the inner ear. This paper reports the clinical motivation, design considerations, analysis, and design optimization of a new robot for electrode arrays insertion. This paper describes a new approach for coordinated insertion of perimodiolar electrode arrays in order to minimize shape discrepancy between the shape of the electrode array and the shape of the inner ear anatomy. A new design of a 3-degrees-of-freedom (DoF) parallel robot with wire-actuated prismatic legs is presented. The dimensional synthesis of the robot design was based on satisfying the accuracy, speed, system size, and workspace requirements. The robot prototype is validated experimentally to execute electrode insertions in plastic models of temporal bones.

Index Terms—Medical robotics, parallel robots, robot kinematics.

I. INTRODUCTION

COCHLEAR implants (CIs) are used to restore auditory sensation in patients with either total or profound hearing loss. This restoration is achieved by delivering direct electrical stimulation to the auditory nerve through an electrode array implanted inside the cochlea. Control of the electrical signal to produce distinguishable auditory sensations is accomplished by an audio receiver and processor worn externally by the CI recipient. As of 2010, there are approximately 71 000 CI recipients in the United States and 219 000 worldwide [1]. A review of CIs history and clinical considerations can be found in [2].

Traditionally, the surgeon performs a mastoidectomy to gain access to the cochlea. The electrode array is then inserted into the scala-tympani (one of three helical chambers in the cochlea). Access into the scala tympani is achieved by either using the round window (a natural opening covered with a membrane) or by drilling a cochleostomy. Different electrode array manufacturers have varying preferences for the opening type depending on the design of a particular electrode. Current clinical practice then has the surgeon manually insert the electrode using a pair of forceps or other electrode-specific manually operated tool [3].

There are many types of electrodes clinically available but all share the characteristic of being thin and delicate structures.

In the case of perimodiolar electrode arrays (PEAs), there is an additional component to the electrode, a thin metal stylet embedded in its silicone body [4]. During the insertion of PEA's, the stylet must be held fixed in space after the first stage of insertion as the electrode is guided deeper into the cochlea, a technique referred to as advance off stylet (AoS).

Complications associated with the insertion of electrode arrays mostly include damage to intracochlear anatomy. The basilar membrane separates the scala tympani and scala media chambers of the cochlea and risks damage during insertion. Several works have investigated trauma to the basilar membrane in histological studies of temporal bone specimens [5]–[8]. Trauma minimization has been emphasized in [6] and [9]. As an increasing number of CI candidates have residual hearing, reducing trauma may help preserve residual hearing. Therefore, the need to minimize trauma will only increase as the CI candidate pool increases.

A review of the current standard of care in CI procedures presents an opportunity for robotics to equip surgeons with an important tool in this operation. This benefit comes from two advantages in a robotic tool. The first is the tool's ability to incorporate accurate positioning, speed control, imaging, and high-resolution force sensing. Human perception of the force is limited to approximately 25 mN [10], [11] and given the small magnitude of forces that may damage intracochlear anatomy, an automated tool will have a lower threshold of perception. The second advantage of a robotic tool is its inherent ability to log all data it perceives during the procedure. This leads to more quantitative metrics in terms of correlating this data to postoperative outcomes. In this regard, robotic insertion systems present an invaluable research platform.

In recent years, there has been several developments in approaching cochlear implantation through the use of robotic tools. A pilot study by Zhang *et al.* [12] used a planar stage and custom-designed steerable electrode for insertion in plastic models of the cochlea. A study of friction in plastic models and the effect of the insertion speed was presented in [13]. Another robot design [14] proposed a custom 6-DoF Stewart–Gough platform for insertion of steerable electrodes in a clinical procedure. Robotic drilling of the mastoidectomy has been presented in [15] and [16] with robotic drilling of the cochleostomy demonstrated in [17] and [18]. The work presented in [19] was a 1-DoF insertion platform for CIs advancing the electrode through a guide tube into the scala tympani. Later, this device incorporated force sensing [20] and insertion in a plastic model against an experienced surgeon was tested [21]. Minimally invasive access to the cochlea using a bone-mounted robotic drill was presented by

The authors are with the Department of Mechanical Engineering, Vanderbilt University, Nashville, TN 37212 USA (e-mail: jason.pile@vanderbilt.edu; nabil.simaan@vanderbilt.edu).
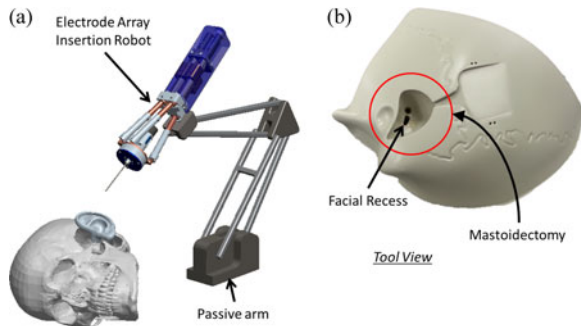
Fig. 1. Robotic insertion concept. (a) After the surgeon has completed the mastoidectomy and gained access to the cochlea, the robotic system is brought to place on a passive arm. Registration to the cochlea can be done with external vision of the cochleostomy or through preoperative image registration [24]. (b) The view of the surgical site from the tool's perspective. The mastoidectomy and small opening through the facial recess restrict tool dimensions and angle of approach. Model temporal bone provided by Cochlear Ltd.

TABLE I
TASK SPECIFICATIONS

Specification	Target Value	Ref.
Targeting accuracy	< 0.4 mm	[24]
Tool Maximum Dia.	2.0 mm	[25]
Insertion speed	0.5 - 5 mm/s	[13], [27]
Insertion force	∼0.05 N	[21], [27], [28]
Angle of approach	6° - 17°	Current Work

Kratchman *et al.* in [22]. Another single-axis automated electrode insertion tool for bench top experimentation has also been presented [23].

The proposed insertion platform (shown conceptually in Fig. 1) aims to address considerations absent from previously proposed designs. Manipulation of the electrode array is preserved in the cochlea's insertion plane while removing 3 DoF from proposed full-spatial mechanisms without compromising control of insertion. For practical future development, isolation of the motors should be considered for sterilization and safety. Our design study focused on variations of the 3RPR planar parallel manipulator incorporating closed-loop wires to remotize the actuator from the surgical site. This gripper incorporates six-axis force sensing and in the case of PEA, an ability to actuate the stylet.

Given the existing body of work, this paper's contributions are threefold: 1) it presents a compilation available information from prior art and addresses workspace knowledge gaps in the literature pertinent to robotic insertion to define a set of design specifications, 2) it introduces a robotic insertion tool with an actuation scheme that isolates actuators from the surgical site with a path forward to clinical implementation, and 3) the kinematics, statics, and stiffness of this robot are modeled and used during the task-based dimensional synthesis process.

II. TASK SPECIFICATION

Table I presents the task specifications used for designing our robot. These task specifications stem from a compilation of various results by other works. This study augments these previous works by experimentally determining the anatomically

available tool orientation workspace. This section describes the methods used for obtaining these task specifications.

The specification for the prototype system are based on information from several sources. The electrode array intended for use with this device is the Contour Advance PEA from Cochlear Ltd. However, this system can readily accept other nonactuated electrodes such as outer wall electrode arrays. The work presented in [24] demonstrated that a targeting accuracy of 0.4 mm at the cochleostomy was sufficient for percutaneous electrode array insertion using a tool rigidly attached to patient's skull without the capability of adjustment during insertion. A study reported in [25] examined the shape of the facial recess through measurements of imaged cross sections of the temporal bone in 200 patients. These results indicated a minimum clearance of 2 mm through the facial recess at its narrowest point which suggests that tools designed to pass through this anatomical constraint should be below this diameter. Zhang *et al.* [13] explored the relationship of the speed and the friction force using outer wall electrodes and found that insertion forces could be reduced by increasing the speed with the reduction seen at speeds as high as 5 mm/s. In [26], an insertion algorithm for perimodiolar electrodes that allowed for freedom in changing the orientation and position of the electrode in a 2-D plane was presented. While [25] provided dimensions of the facial recess, which guided the dimensioning of the electrode gripper tip; it did not characterize the allowable electrode insertion approach angles. The anatomy of the facial recess limits the orientation workspace of the robot gripper. This information about the orientation workspace is an important design specification that has not been characterized in the literature.

An experiment was designed to obtain an accurate specification for the allowable orientation workspace for CI surgery. For this experiment, a tool was constructed with the same dimensions as the proposed device's electrode gripper and tested the available angular workspace on ten human cadaveric temporal bone specimens. An NDI Polaris Vicra optical tracker was used to collect position and orientation information on the tool. The Vicra has a working range between 0.5 and 1.3 m and an RMS accuracy of 0.25 mm. The tool tip was placed at the cochleostomy and measurements were taken as the tool was pivoted about the cochleostomy to trace the angular limitations of the facial recess. For each bone, ten trials were conducted with roughly 600 data points taken per trial. A convex hull method [29] was used to reconstruct the continuous curve enclosing the allowable angular straight line access to the cochlea.

Fig. 2 shows a polar plot of the available tool tilting workspace for all temporal bones. The radial distance of each point on a given closed curve provides the maximal tilt angle at a given tilt direction, designated in the plot by the polar coordinate. The figure shows a high variability of maximal tilting range. Note that all curves have been plotted such that their major axes align along the 0° tilt direction. The major axis aligned with our proposed 2-D insertion plane.

The results show that the minimal angular tilting workspace was 6° and the maximal range was 17°. Note that the insertion path planning in [26] showed that tilting angles of up to 20° were able to reduce the shape discrepancy between the equilibrium
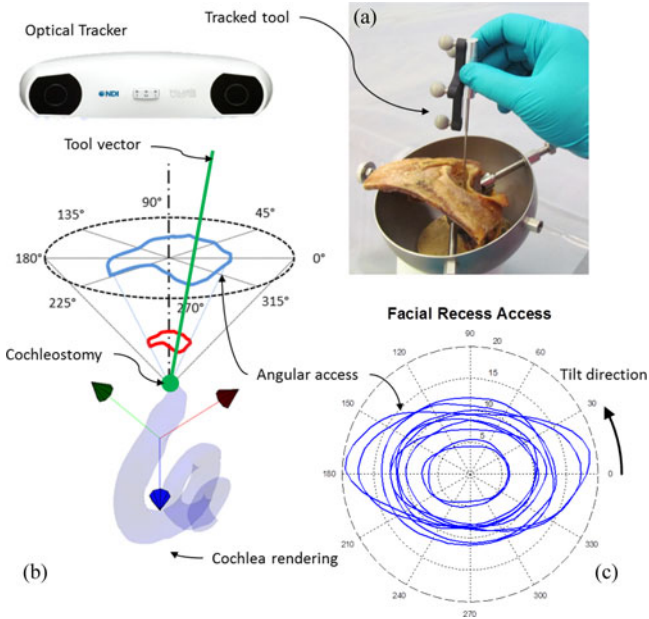
Fig. 2.   Experimental validation of facial recess access. (a) A tracked tool with diameter comparable to the proposed insertion robot's gripper pivots about cochleostomy of ten human temporal bones. (b) For each temporal bone, an angular access perimeter is defined by tracing the limits imposed by the facial recess. (c) The results show minimal access of $6°$.
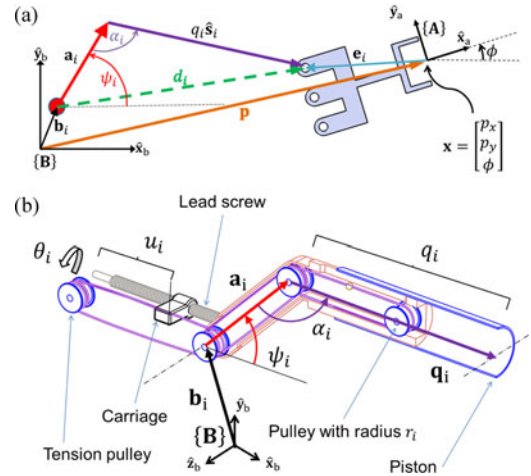

Fig. 3.   Kinematic diagram for 3RPR manipulator. (a) One of the three kinematic chains is shown schematically for the 3RPR design. (b) The prismatic link is actuated through a closed-loop wire rope. This approach allows the motors to be placed at an arbitrary distance from the link. The motors drive a carriage on a leadscrew which transmits motion to the piston.

shape of the PEA and the scala tympani of the cochlea. The results of these temporal bone experiments were adopted as a design specification since the proposed path planner can restrict tilting angles to meet the constraints of more restrictive facial recess anatomies.

III. GENERALIZED MECHANICAL ARCHITECTURE

The insertion robot uses a planar 3-DoF parallel kinematic structure with a fourth actuator mounted on the end effector for stylet actuation for several reasons. A planar structure matches the kinematic description of the PEA insertion process [3], [26] and the approximate 2-D model of the cochlea [30], [31] without added complexity. A parallel mechanism was chosen to control PEA placement due to its advantages in precision, compactness, and stiffness [32]. Finally, forces acting on the PEA must be transmitted completely through the force transducer. This necessitates having a separate actuator on the end effector.

Among various configurations of planar parallel mechanisms, a design was chosen based on the 3RPR configuration: three parallel actuated prismatic links connected to the robot base and end effector with revolute joints. This type of kinematic chain leads to a compact form factor and allows exploration of wire actuation concepts which, to the best of the authors' knowledge, has not been applied to planar, piston-driven parallel mechanisms.

The kinematic definition of one of the three chains is shown in Fig. 3(a). Force transmission between the motors and the moving platform is accomplished through a tensioned wire loop for each leg [see Fig. 3(b)]. Motor rotation was transferred to wire translation through a lead screw. While this adds length to the device for the screw/nut travel it was incorporated into

the design for two considerations. 1) The motor assemblies need a right angle connection to minimize the cross-sectional footprint of the device. 2) backlash in the motor gearheads (necessary for compact motors) leading to position errors is reduced in proportion to the pitch of the lead screw used. Future designs will remove this intermediate step and connect the wire loop to a capstan coupled to the motor output shafts for further compactness.

Wire actuation was selected over rigid transmission elements to enable motor isolation and to have greater control over weight distribution. Another significant advantage is that wires have greater potential for miniaturization in comparison to lead screws and other linear motion mechanisms which would be found inside the prismatic links. The concessions made in using wire rope for this application include a reduction in joint stiffness and a smaller load capacity. The internal friction [33] may necessitate nonlinear compensation. Also, fatigue on wire rope can lead to breakage and as a result need more disciplined maintenance. Since cochlea insertion forces generally do not exceed 0.5 N, the stiffness and capacity losses were not expected to significantly disrupt the performance.

IV. MODELING AND ANALYSIS

Position control of the parallel robot is accomplished using a closed-form inverse position solution. The linearized instantaneous kinematics of the robot is used in performance analysis, calibration, and for real-time regulation of position based on limitations of the actuators, joints, and task space constraints. The derivation of the kinematics and the effects of wire actuation are presented in this section.

In the following modeling framework, we will neglect extension of the actuation wires. This simplification is justified if the actuation wires are sufficiently pretensioned and the actuation forces during the normal operation are small compared to the pretensioning loads. This device carries only minimal load

(less than 90 g) and is subject to negligible external forces from the PEA. Additional positioning errors may be corrected by applying hybrid force/position control in the future.

Fig. 3(a) shows the kinematic model of one kinematic chain of the robot. Unless otherwise explicitly stated, all vectors will be described in the robot base frame $\{\mathbf{B}\}$. The motor input is described by a vector $\boldsymbol{\theta} = [\theta_1, \theta_2, \theta_3]^{\mathrm{T}}$. Motor rotations θ_i correspond with linear translations u_i of wire-carriages by using lead screws and nuts. The task space configuration is defined at the tip of the electrode array gripper by $\mathbf{x} = [p_x, p_y, \phi]^{\mathrm{T}}$. The active joint variables $\mathbf{q} = [q_1, q_2, q_3]^{\mathrm{T}}$ designate the piston strokes. The fourth degree of actuation is employed specifically for the perimodiolar electrode which require the coordinated pulling of the embedded stylet during the insertion process. Pulling of the stylet is denoted by q_s.

A. Inverse Position Analysis

Given the gripper pose $\mathbf{x} = \left[\mathbf{p}^{\mathrm{T}}, \phi\right]^{\mathrm{T}}$, the inverse kinematic solution is found using loop closure of the kinematic chains. Vectors $\mathbf{b}_i$ in Fig. 3 define the location of the ith fixed revolute joint in the robot base frame. Vectors $\mathbf{a}_i = [\cos(\psi_i), \sin(\psi_i), 0]^{\mathrm{T}}$ define the mechanical offset of the piston axis from the ith fixed revolute joint and the distances a_i are defined as $a_i = \|\mathbf{a}_i\|$. The piston stroke is defined by $\mathbf{q}_i = q_i \hat{\mathbf{s}}_i$. The angles α_i are the fixed interior angles between the piston axis $\hat{\mathbf{s}}_i$ and $\mathbf{a}_i$. The ith revolute joint on the moving platform connects to the piston tip. Vectors $\mathbf{e}_i$ connect the gripper point $\mathbf{p}$ to the ith revolute joint of the moving platform.

To write loop closure equations, we define vectors $\mathbf{d}_i$ from the ith fixed revolute joint to the corresponding revolute joint in the moving platform (see Fig. 3). We then solve the following loop closure equation for $\mathbf{d}_i$:

$$\mathbf{p} + \mathbf{e}_i - \mathbf{d}_i - \mathbf{b}_i = \mathbf{0}. \tag{1}$$

Given $\mathbf{d}_i$, the piston stroke can be found using the cosine triangle identity

$$q_i = a_i \cos(\alpha_i) \pm \sqrt{a_i^2 \cos^2(\alpha_i) - a_i^2 + d_i^2} \tag{2}$$

and through completing the triangle, the vectors $\mathbf{a}_i$ and $\mathbf{q}_i$ are known. Given $\mathbf{d}_i$ and q_i, ψ_i is obtained using the law of sines

$$\psi_i = \operatorname{atan2}(d_{y,i}, d_{x,i}) + \arcsin\left(\frac{q_i}{d_i \sin(\alpha_i)}\right). \tag{3}$$

Due to the wire actuation, the piston strokes q_i are coupled with ψ_i based on the radius of the wire rope pulley r_i and the translation of the wire carriages u_i. We assume a known home configuration with values $q_{i,\mathrm{home}}$, $\psi_{i,\mathrm{home}}$, and $\theta_{i,\mathrm{home}}$. Also, we assume that the lead screws have a known lead η_i and the carriage displacement u_i is given by $u_i = \eta_i(\theta_i - \theta_{i,\mathrm{home}})$. We define $\mathbf{R} = \operatorname{diag}^1([r_1, r_2, r_3])$ and $\mathbf{G} = \operatorname{diag}([\frac{1}{\eta_1}, \frac{1}{\eta_2}, \frac{1}{\eta_3}])$ as the pulley radius and transmission gain matrices, respectively. Using these definitions, the kinematic compatibility of the inextensible wire loop is given by

$$\mathbf{G}^{-1}(\boldsymbol{\theta} - \boldsymbol{\theta}_{\mathrm{home}}) + \mathbf{R}(\boldsymbol{\psi} - \boldsymbol{\psi}_{\mathrm{home}}) = \mathbf{q} - \mathbf{q}_{\mathrm{home}}. \tag{4}$$

---
[1] $\operatorname{diag}(\mathbf{a})$ is the diagonalization of vector $\mathbf{a}$

Finally, the motor rotations $\boldsymbol{\theta}$ are found using (4).

B. Instantaneous Kinematics and Statics

The instantaneous kinematics is useful for evaluating the quality of the mechanism, for control algorithms, and for calibration. Using the approach of [34], we start by writing the loop closure equations of the kinematic chains

$$\mathbf{b}_i + \mathbf{a}_i + \mathbf{q}_i = \mathbf{p} + \mathbf{e}_i. \tag{5}$$

Taking the time derivative of both sides of (5) yields

$$\dot{q}_i \hat{\mathbf{s}}_i + \dot{\psi}_i(\hat{\mathbf{z}}_b \times (\mathbf{a}_i + q_i \hat{\mathbf{s}}_i)) = \dot{\mathbf{p}} + \dot{\phi}(\hat{\mathbf{z}}_b \times \mathbf{e}_i). \tag{6}$$

First, the relationship between the task space velocity $\boldsymbol{\zeta}$ and piston velocity $\dot{\mathbf{q}}$ is found by eliminating $\dot{\psi}$ from (6). This is accomplished by premultiplying (6) by $(\mathbf{a}_i + q_i \hat{\mathbf{s}}_i)^{\mathrm{T}}$ and simplifying using triple product rules

$$\mathbf{J}_q \dot{\mathbf{q}} = \mathbf{J}_\zeta \boldsymbol{\zeta} \tag{7}$$

where $\mathbf{J}_q$, $\mathbf{J}_\zeta$ is given by

$$\mathbf{J}_q = \operatorname{diag}\left(\left[\mathbf{a}_1^{\mathrm{T}} \hat{\mathbf{s}}_1 + q_1, \mathbf{a}_2^{\mathrm{T}} \hat{\mathbf{s}}_2 + q_2, \mathbf{a}_3^{\mathrm{T}} \hat{\mathbf{s}}_3 + q_3\right]\right) \tag{8}$$

$$\mathbf{J}_\zeta = \begin{bmatrix} (\mathbf{a}_1 + q_1 \hat{\mathbf{s}}_1)^{\mathrm{T}} & [\mathbf{e}_1 \times (\mathbf{a}_1 + q_1 \hat{\mathbf{s}}_1)]^{\mathrm{T}} \hat{\mathbf{z}}_b \\ (\mathbf{a}_2 + q_2 \hat{\mathbf{s}}_2)^{\mathrm{T}} & [\mathbf{e}_2 \times (\mathbf{a}_2 + q_2 \hat{\mathbf{s}}_2)]^{\mathrm{T}} \hat{\mathbf{z}}_b \\ (\mathbf{a}_3 + q_3 \hat{\mathbf{s}}_3)^{\mathrm{T}} & [\mathbf{e}_3 \times (\mathbf{a}_3 + q_3 \hat{\mathbf{s}}_3)]^{\mathrm{T}} \hat{\mathbf{z}}_b \end{bmatrix}. \tag{9}$$

The relationship between $\boldsymbol{\zeta}$ and $\dot{\mathbf{q}}$ can be written as

$$\dot{\mathbf{q}} = \mathbf{J}_q^{-1} \mathbf{J}_\zeta \boldsymbol{\zeta} = \mathbf{J}_{q\zeta} \boldsymbol{\zeta}. \tag{10}$$

Due to wire routing, the piston strokes are not independent of each other. Decoupling relationships are required to relate $\dot{\boldsymbol{\theta}}$ to $\boldsymbol{\zeta}$. The time derivative of (4) is

$$\dot{\boldsymbol{\theta}} = \mathbf{G}(\dot{\mathbf{q}} - \mathbf{R}\dot{\boldsymbol{\psi}}). \tag{11}$$

The relationship between $\dot{\boldsymbol{\psi}}$ and $\boldsymbol{\zeta}$ is obtained by substituting $\mathbf{d}_i = \mathbf{a}_i + q_i \hat{\mathbf{s}}_i$ into (6)

$$\dot{\psi}_i [\hat{\mathbf{z}}_b \times \mathbf{d}_i] + \dot{q}_i \hat{\mathbf{s}}_i = \dot{\mathbf{p}} + \dot{\phi}[\hat{\mathbf{z}}_b \times \mathbf{e}_i] \tag{12}$$

premultiplying (12) by $[\hat{\mathbf{z}}_b \times \mathbf{d}_i]^{\mathrm{T}}$, and with the simplification $[\hat{\mathbf{z}}_b \times \mathbf{d}_i]^{\mathrm{T}}[\hat{\mathbf{z}}_b \times \mathbf{e}_i] = \mathbf{d}_i^{\mathrm{T}} \mathbf{e}_i$ for the planar mechanism, we obtain

$$\dot{\boldsymbol{\psi}} = (\mathbf{J}_1 \mathbf{J}_{q\zeta} + \mathbf{J}_2)\boldsymbol{\zeta} = \mathbf{J}_{\psi\zeta} \boldsymbol{\zeta} \tag{13}$$

where

$$\mathbf{J}_1 = \operatorname{diag}\left(\left[\frac{[\hat{\mathbf{z}}_b \times \mathbf{d}_1]^{\mathrm{T}} \hat{\mathbf{s}}_1}{\mathbf{d}_1^{\mathrm{T}} \mathbf{d}_1}, \quad \frac{[\hat{\mathbf{z}}_b \times \mathbf{d}_2]^{\mathrm{T}} \hat{\mathbf{s}}_2}{\mathbf{d}_2^{\mathrm{T}} \mathbf{d}_2}, \quad \frac{[\hat{\mathbf{z}}_b \times \mathbf{d}_3]^{\mathrm{T}} \hat{\mathbf{s}}_3}{\mathbf{d}_3^{\mathrm{T}} \mathbf{d}_3}\right]\right)$$

$$\mathbf{J}_2 = \begin{bmatrix} \frac{[\hat{\mathbf{z}}_b \times \mathbf{d}_1]^{\mathrm{T}}}{\mathbf{d}_1^{\mathrm{T}} \mathbf{d}_1} & \frac{\mathbf{d}_1^{\mathrm{T}} \mathbf{e}_1}{\mathbf{d}_1^{\mathrm{T}} \mathbf{d}_1} \\ \frac{[\hat{\mathbf{z}}_b \times \mathbf{d}_2]^{\mathrm{T}}}{\mathbf{d}_2^{\mathrm{T}} \mathbf{d}_2} & \frac{\mathbf{d}_2^{\mathrm{T}} \mathbf{e}_2}{\mathbf{d}_2^{\mathrm{T}} \mathbf{d}_2} \\ \frac{[\hat{\mathbf{z}}_b \times \mathbf{d}_3]^{\mathrm{T}}}{\mathbf{d}_3^{\mathrm{T}} \mathbf{d}_3} & \frac{\mathbf{d}_3^{\mathrm{T}} \mathbf{e}_3}{\mathbf{d}_3^{\mathrm{T}} \mathbf{d}_3} \end{bmatrix}. \tag{14}$$

If $\mathbf{d}_i$ and $\hat{\mathbf{s}}_i$ are collinear, then $\dot{q}_i [\hat{\mathbf{z}}_b \times \mathbf{d}_i]^{\mathrm{T}} \hat{\mathbf{s}}_i = 0$ and $\mathbf{J}_1 = \mathbf{0}$. Using (11), $\dot{\boldsymbol{\theta}}$ is given by

$$\dot{\boldsymbol{\theta}} = \mathbf{G}(\mathbf{J}_{q\zeta} - \mathbf{R}\mathbf{J}_{\psi\zeta})\boldsymbol{\zeta} = \mathbf{J}_{\theta\zeta} \boldsymbol{\zeta}. \tag{15}$$
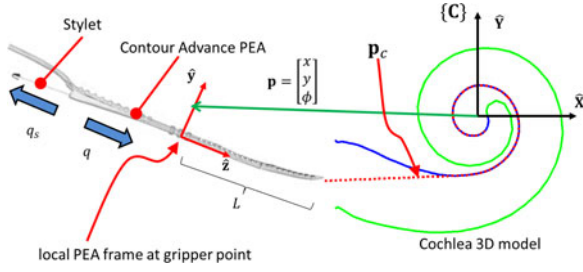
Fig. 4. Insertion kinematics schematic. The rendered cochlea model is not to scale compared to PEA. The dashed line within the 2-D cochlea represents the desired path of the PEA.

Using the instantaneous kinematics, a first-order approximation of the loads transmitted from the end effector to the motor is made. Fig. 3(b) shows the constant-length wire loop transmitting the force between the actuator and the piston. Using the virtual work method [34] and neglecting the piston weight, the statics of the robot can be written as

$$\boldsymbol{\tau}_\theta^{\mathrm{T}} \delta\boldsymbol{\theta} = \boldsymbol{\tau}_\theta^{\mathrm{T}} \mathbf{J}_{\theta\zeta} \delta\mathbf{x} = \mathbf{w}^{\mathrm{T}} \delta\mathbf{x} \tag{16}$$

where $\mathbf{w}$ represents the wrench acting on the end effector (a two-component force in plane $\hat{\mathbf{x}}_b \hat{\mathbf{y}}_b$ and a moment about $\hat{\mathbf{z}}_b$) and $\boldsymbol{\tau}_\theta$ is the vector of motor torques. Using (16), we obtain

$$\boldsymbol{\tau}_\theta = \left(\mathbf{J}_{\theta\zeta}^{\mathrm{T}}\right)^{-1} \mathbf{w}. \tag{17}$$

V. INSERTION PATH PLANNING

The path planning algorithm is based on a combination of the electrode kinematic behavior and a 2-D model estimation as detailed in [26]. The parameter values can be specified using a general model as proposed in [30] or based on preoperative CT data as demonstrated in [24]. The inner and outer walls of the scala tympani are reconstructed in a 2-D plane using spline curves. Fig. 4 depicts the kinematic model. Through this section, the pose of the PEA base frame $\mathbf{p}$ is written in the cochlea frame $\{\mathbf{C}\}$. A PEA can be modeled as a curve whose shape is determined by the instantaneous tangent angle $\theta_e(s, q_s)$, where s is the arc length of the PEA's inner (modiolar) edge and q_s is the actuation of the stylet. Positive values of q_s indicate stylet retraction. From our prior PEA study [26], a 16 element calibration matrix $\mathbf{A}$ can be measured and the shape of the electrode can be written as

$$\theta_e(s, q_s) = \boldsymbol{\psi}_{\mathbf{e}}(s)^{\mathrm{T}} \mathbf{A} \boldsymbol{\eta}_e(q_s) \tag{18}$$

where

$$\boldsymbol{\psi}_{\mathbf{e}}(s) = \begin{bmatrix} 1, & s, & s^2, & s^3 \end{bmatrix}^{\mathrm{T}}$$
$$\boldsymbol{\eta}_e(q_s) = \begin{bmatrix} 1, & q_s, & q_s^2, & q_s^3 \end{bmatrix}^{\mathrm{T}}. \tag{19}$$

For optimal insertion, the PEA should fit the shape of the scala tympani by approximating the modiolar (inner) wall as much as possible while avoiding contact with the lateral (outer) wall. The desired path for the PEA tip begins as a straight line from the entry point to the scala tympani toward the modiolar wall intersecting at the closest point of tangency. Let the points along this path be given by Cartesian coordinates $\mathbf{p}_c(s) \in \mathbb{R}^{2\times 1}$. Let z

digitized points along the electrode array be given by Cartesian coordinates $\mathbf{p}_e(s) \in \mathbb{R}^{2\times 1}$. During insertion, the focus is on the inserted portion of the electrode array; hence, we define a weight matrix $\mathbf{W} = \mathrm{diag}(0 \ldots \mathrm{w}, \mathrm{w}, \mathrm{w}, \mathrm{w}) \in \mathbb{R}^{2z\times 2z}$, where the scalar weight w is used for points that are inside the scala tympani and a zero value for points not yet inserted into the scala tympani. We define an objective function for each insertion depth d such that a penalty is applied for deviation from the desired path and an additional penalty is applied for violating the modiolar wall boundary

$$\underset{d,\phi}{\mathrm{argmin}} \frac{1}{2} \left(\mathbf{T}^{\mathrm{T}} \mathbf{W} \mathbf{T} + \mathbf{U}^{\mathrm{T}} \mathbf{W} \mathbf{U}\right) \tag{20}$$

where the vectors $\mathbf{T}$ and $\mathbf{U}$ are given by

$$\mathbf{T} = \begin{bmatrix} \mathbf{p}_c(s=0) - \mathbf{p}_e(d, \phi, s=0) \\ \vdots \\ \mathbf{p}_c(s=L) - \mathbf{p}_e(d, \phi, s=L) \end{bmatrix} \in \mathbb{R}^{2z\times 1} \tag{21}$$

$$\mathbf{U} = \begin{bmatrix} u_e(s=0), & \cdots, & u_e(s=L) \end{bmatrix}^{\mathrm{T}} \in \mathbb{R}^{2z\times 1}. \tag{22}$$

The value of $u_e(s)$ indicates the interference distance for each digitized point along the electrode array (23).

The vectors $\mathbf{r}_e(s)$ and $\mathbf{r}_c(s)$, respectively, denote the radial distances from the center of the cochlea to a point on the PEA specified by arc length s and the closest corresponding point on the scala tympani inner wall

$$\underset{s\in[0,L]}{u_e(s)} = \begin{cases} \|\mathbf{r}_c(s) - \mathbf{r}_e(s)\|, & \text{if } \|\mathbf{r}_c(s)\| > \|\mathbf{r}_e(s)\| \\ 0, & \text{if } \|\mathbf{r}_c(s)\| \le \|\mathbf{r}_e(s)\|. \end{cases} \tag{23}$$

During the simulation, the insertion depth d was set for 15 mm in 0.5 mm increments. Optimal position and orientation of the electrode array base were determined at each increment using a line search optimization method. The base location and orientation of the simulated electrode define the end effector path of the robot. A cubic spline interpolation was used for evaluating intermediate positions along the trajectory.

VI. DIMENSIONAL SYNTHESIS

The dimensional synthesis of our mechanism was defined with the aim of determining the kinematic parameters that minimize sensitivity to actuation error while making efficient use of the piston stroke and minimizing the actuator power. We cast this as a constrained minimization problem solving for the leg lengths a_i and $^A\mathbf{e}_i = [e_{x,i}, e_{y,i}, 0]^{\mathrm{T}}$ for a total of nine design parameters. Vectors $\mathbf{b}_i$ were predefined due to the size limitations. The final prototype used $\alpha_i = \pi$ for manufacturing cost considerations. The simulated insertion trajectories were discretized into 100 sample poses per insertion path and used to define the workspace $\mathbb{W}$ over which the following cost function was calculated:

$$f\left(a_i, {}^A\mathbf{e}_i\right)_{\mathrm{obj}} = f_{\mathrm{err}} + f_{\mathrm{leg}} + f_{\mathrm{power}} \tag{24}$$

where f_{err}, f_{leg}, and f_{power} are defined in the following sections. The reader should refer to Table II for parameters used in evaluating the optimization function.

TABLE II
OPTIMIZATION PARAMETERS

Variable	Units	Range/Value	Variable	Units	Value
a_i	mm	$[10, 80]$	ϵ_x	mm	0.4
e_x	mm	$[-100, -50]$	ϵ_y	mm	0.4
e_y	mm	$[-25, 25]$	ϵ_ϕ	deg	0.3
$\delta\theta$	rad	0.2	p_{max}	mW	75
$\tilde{a}$	mm	20	λ_c	mm^{-1}	0.5

A. Error Sensitivity

The sensitivity analysis determines the maximal end effector pose error $\delta\mathbf{x}$ stemming from a bounded motor input error $\delta\boldsymbol{\theta}$ such that $\delta\theta_i \in [\theta_i - \zeta_\theta, \theta_i + \zeta_\theta]$. Instead of using error ellipsoids assuming norm-bounded error $\delta\boldsymbol{\theta}$ we used the more conservative error polytopes [35] where we assumed that each actuator has a bounded error stemming from backlash. The maximal expected pose error is approximated by

$$\delta\mathbf{x}\,(\delta\boldsymbol{\theta}) = \operatorname{argmax}\left(\mathbf{J}_{\zeta\theta}\delta\boldsymbol{\theta}\right),\; \delta\theta_i \in [-\zeta_\theta, \zeta_\theta]. \quad (25)$$

A weighted objective function f_{err} quantifying the weighted norm of the end effector error was defined as follows:

$$f_{\mathrm{err}} = \delta\mathbf{x}^{\mathrm{T}}\mathbf{W}\delta\mathbf{x}. \quad (26)$$

The weight matrix $\mathbf{W} = \operatorname{diag}([\frac{1}{\epsilon_x}, \frac{1}{\epsilon_y}, \frac{1}{\epsilon_\phi}])$ addresses dimensionality by scaling the three components of $\delta\mathbf{x}$ by their respective desired accuracy requirements defined in Table II.

B. Power Requirements

The function f_{power} quantifies the average peak power across all insertion runs and discourages design solutions with rapid motion through sections of the insertion trajectory. For ith leg ($i = 1, 2, 3$) and the jth pose ($j = 1, 2, \ldots, 100$) along a given insertion path, we calculate $\tau_{\theta,i,j}$ and $\dot{\theta}_{i,j}$ assuming an insertion rate of 1 mm/s. The instantaneous power is calculated and normalized by the maximal actuator power $p_{w,\max}$. We define the vector $\mathbf{p}_w$ with elements $p_{w,k}$ ($k = 1, 2, \ldots, n$) representing the maximal required normalized power for all insertion paths in $\mathbb{W}$. Using these definitions, the objective function f_{power} is given by

$$f_{\mathrm{power}} = \left(\mathbf{p}_w^{\mathrm{T}}\mathbf{p}_w\right)/n \quad (27)$$

where $n = 28$ is the number of insertion paths, and $p_{w,j}$ is

$$p_{w,k} = \operatorname{argmax}((\tau_{\theta,i,j}\,\dot{\theta}_{i,j})/p_{w,\max}). \quad (28)$$

C. Piston Stroke Utilization

The objective function f_{leg} guides the design to avoid exceeding the feasible piston strokes. Also, an ideal design uses the entire available stroke in each leg. We thus define this function as a sum of three positive-definite functions

$$f_{leg} = \mathbf{f}_1^{\mathrm{T}}\mathbf{f}_1 + \mathbf{f}_2^{\mathrm{T}}\mathbf{f}_2 + \mathbf{f}_3^{\mathrm{T}}\mathbf{f}_3. \quad (29)$$

Across all simulated insertion trajectories, a minimum and maximum piston position $q_{i,\min}$ and $q_{i,\max}$ is determined for each leg with their difference defined as $\Delta q_i = q_{i,\max} - q_{i,\min}$. Let the constant $\tilde{a}_i$ designate a portion of the initial leg length that
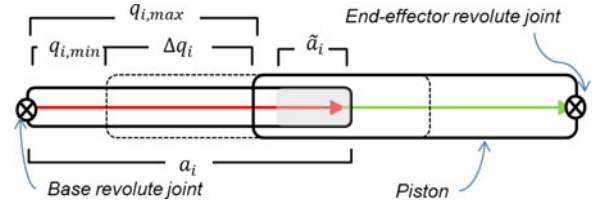

Fig. 5. Stroke utilization and stroke limits. Solid/dashed line designates a fully extended/retracted piston.

TABLE III
KINEMATIC PARAMETERS AND THE EXPECTED PERFORMANCE

Parameter	Value as built	Metric	Est. Performance
$[a_1, a_2, a_3]$	$\begin{bmatrix} 63.2 & 63.2 & 64 \end{bmatrix}$	$\delta\mathbf{x}$	$\begin{matrix} 0.02mm \\ 0.34mm \\ 0.1° \end{matrix}$
$[\mathbf{b}_1, \mathbf{b}_2, \mathbf{b}_3]$	$\begin{matrix} 0, 0, 0 \\ 8, -8, 0 \end{matrix}$	Max p_w	$< 3mW$
$[\mathbf{e}_1, \mathbf{e}_2, \mathbf{e}_3]$	$\begin{matrix} -88, -88, -88 \\ -2, -21, 21 \end{matrix}$	Stroke	$[0.61, 0.86, 0.58]$

must be reserved for mechanical assembly, and let $\bar{q}_{i,\min} = 0$ and $\bar{q}_{i,\max} = a_i - \tilde{a}_i$ designate the feasible upper and lower bounds of the piston stroke. Using these definitions, we present the rationale behind defining $\mathbf{f}_1, \mathbf{f}_2, \mathbf{f}_3$ used in (29).

Stroke utilization was defined as the unused portion of the minimal required leg length. In the constructed prototype, $\mathbf{a}_i$ and $\mathbf{q}_i$ (see Fig. 5) are collinear, and the stroke utilization metric $\mathbf{f}_1 \in \mathbb{R}^{3\times 1}$ is defined with it components given by

$$f_{1,i} = 1 - \Delta q_i/\bar{q}_{i,\max}. \quad (30)$$

In addition to stroke utilization, we wish to guide the synthesis toward mechanically feasible designs where the minimal length is zero or positive, and the stroke does not exceed feasible limits. This is achieved by demanding that $q_{i,\min} \in [0, \bar{q}_{i,\max}]$ and $\Delta q_i \in [0, \bar{q}_{i,\max} - q_{i,\min}]$. Given a stroke interval with a minimum (c_0) and a maximum (c_1), the cost function is defined as

$$c(x, c_0, c_1) = \lambda_c \left(\sqrt{(x^2 - c_0)^2 + \epsilon} \right.$$
$$\left. + \sqrt{(x^2 - c_1)^2 + \epsilon} + c_0 - c_1 \right). \quad (31)$$

This function is zero within the interval and increases linearly outside the interval. The small value, ϵ, allows smooth differentiation during numerical optimization. The constant $\lambda_c > 0$ scales the penalty per unit distance. The functions $\mathbf{f}_2, \mathbf{f}_3 \in \mathbb{R}^{3\times 1}$ are defined with their components given by $f_{2,i} = c(q_{i,\min}, 0, \bar{q}_{i,\max})$ and $f_{3,i} = c(\Delta q_i, 0, \bar{q}_{i,\max} - q_{i,\min})$.

D. Optimization Constraints and Results

Results of this optimization are given in Table III. It must be noted that practical limitations for the device geometry, including the dimensions of the available force sensor, place limits on the available configurations where a local minima in the objective function was not reached. The expected performance
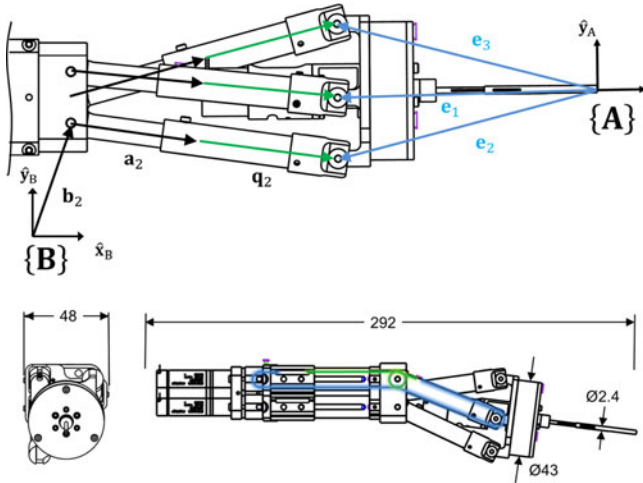
Fig. 6. Robotic insertion tool's key dimensions shown without protective coverings. All vectors are labeled along the second kinematic chain while some labels are omitted in the other chains for image clarity. The overlayed curve in the side view shows the routing of the wire rope to actuate joint 1. Dimensions are in millimeters.
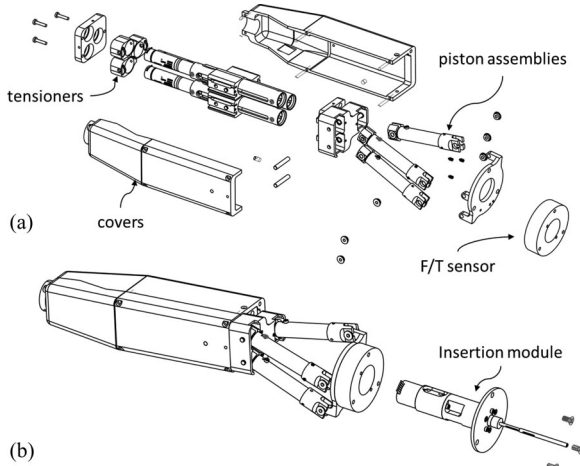

Fig. 7. Prototype Assembly. (a) The 3-DoF wire-actuated platform was assembled with the force/torque sensor attached as shown. (b) The insertion module is attached separately.

measures, also included in Table III, are based on the dimensions of the system as built.

Fig. 6 overlays the kinematic vectors of Fig. 3 on the rendering of the robotic system. In this image, the pistons are extended so that vectors $\mathbf{q}_i$ are clearly visible.

VII. PHYSICAL DESIGN AND EVALUATION

A. Mechanical assembly

The fabricated prototype (see Figs. 6 and 7) is 292 mm long and weighs approximately 450 g. An ATI Nano43 6 axis force/torque (F/T) sensor was used to hold an end-effector, consisting of the stylet actuator and a gripper. A rendering of the robotic system with principle dimensions is shown in Fig. 6 along with the wire rope routing required to link the actuators to the pistons. The wire rope employed in this device is a stainless steel Type-S construction available from Asahi Intecc. After
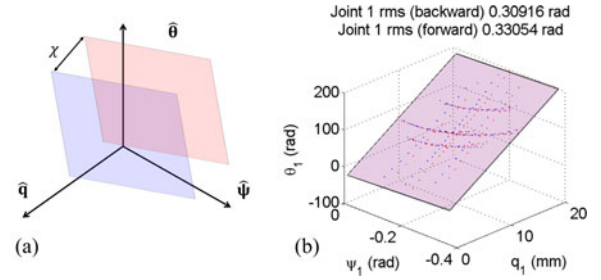

Fig. 8. Joint-level kinematics and backlash. Piston extension q_i, arm rotation angle ψ_i, and motor input θ_i are linearly related in the kinematic model. (a) An unknown degree of backlash χ_i creates two planes of motion dependent on the direction of motion in the actuator. (b) Sample calibration results for joint 1.

routing, the wire rope must be conditioned by cycling it through the device's range of motion and continually retensioning it to take up any slack. The robot controller runs on an Advantech pc104 (500 MHz) single board computer with a Sensoray 526 data acquisition card supporting 16-bit analog input to collect measurements from the Nano43 sensor. The MATLAB xPC Target package was used as the real-time OS running low-level motor control and force data acquisition. The three pistons use 16:1 gearhead servomotors with peak power of 1.5W (Maxon Motors P/N 256105) and lead screws with 0.61-mm pitch. The stylet is actuated by a 37:1 geared, brushed motor from Micromo (P/N 1506N003SR).

B. Calibration and Backlash Compensation

Calibration was used to identify kinematic parameters a_i, η_i, r_i and the degree of backlash, quantified by χ_i, in the robot. The parameters $\mathbf{b}_i$, $\mathbf{e}_i$, and $\boldsymbol{\alpha}_i$ are verified during the fabrication process. From (4), it can be seen that η_i and r_i define a plane in the space $\{\hat{\boldsymbol{\psi}}, \hat{\mathbf{q}}, \hat{\boldsymbol{\theta}}\}$. Backlash results in motion on two parallel planes in this space, separated by χ_i [see Fig. 8(a)] and is dependent on the direction of piston motion. The motion direction of the ith leg and kth measured pose in a sequence of movements is defined by $m_{i,k} \in \mathbb{R}^{3 \times 1}$, where

$$m_{i,k} = \begin{cases} 1, & q_{i,k} > q_{i,k-1} \\ 0, & q_{i,k} < q_{i,k-1}. \end{cases} \tag{32}$$

Calibration begins by returning the system to its home configuration ($q_i = 0, \psi_i = \psi_0, \theta_i = \theta_0, \mathbf{m} = \mathbf{0}$) and then moving through a sequence of 300 poses $\mathbf{x}_k, k = [1, \dots, 300]$. The Polaris Vicra optical tracker was used to measure the relative transformations of the end effector to the robot base. Tracking markers were embedded into the covers of the tool to define the base frame of the robot and to later register the device to the surgical environment. Using (5), the value of the measured piston extensions, $\mathbf{q}_k$, was determined. Values recorded from the controller include motor positions $\boldsymbol{\theta}_k$ and the motor direction $\mathbf{m}_k$. The error between measured and the expected piston stroke are written as $\Delta q_{i,k} = q_{i,k} - q_{i,0} = q_{i,k}$. Defining $\Delta \theta_{i,k} = \theta_{i,k} - \theta_{i,0}$ and $\Delta \psi_{i,k} = \psi_{i,k} - \theta_{i,0}$, each kinematic chain has its experimental data separated according to the motor direction. A plane is then fitted to the separate datasets for each leg using

TABLE IV
SYSTEM PERFORMANCE QUANTIFICATION

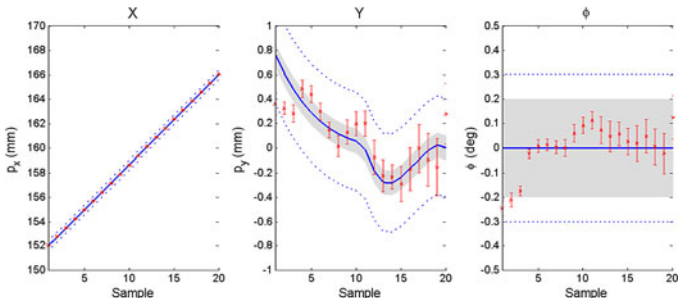|	Positional Repeatability	Positional Accuracy
p_x (mm rms)	$0.02mm$	$0.1mm$
p_y (mm rms)	$0.13mm$	$0.8mm$
ϕ (deg rms)	$0.04°$	$0.25°$

Fig. 9. Position tracking post calibration. Solid line represents desired trajectory, grey area represents tracker uncertainty, and points with error bars show average position and deviation of tracked end effector using ten trials.

orthogonal regression satisfying

$$\Delta\theta_i = \left(\left.\frac{1}{\eta_i}\right|_{m_{i,k}} \right) q_i - \left(\left.\frac{r_i}{\eta_i}\right|_{m_{i,k}} \right) \Delta\psi_i - \chi_i|_{m_{i,k}} .$$

Fig. 8(b) presents a graphical representation of the fitting process and shows collected data from the first kinematic chain. Although the fitting in (33) allows for different values of r_i and η_i depending on $m_{i,k}$, in practice, the coefficients are constant within the measurement noise and provide additional validation to the calibration model. The RMS error for the planar fitting was below 0.6 rad in each chain. With a uniform actuator transmission ratio of $\eta_i = 0.097$ mm/rad, the fitting error was below the 0.1 mm q_i error assumed during the design synthesis phase. Once χ_i is known, it is applied to the controller to adjust $\boldsymbol{\theta}$ based on $\mathbf{m}$.

C. Performance Quantification

The task space positioning accuracy and repeatability were tested after calibration. Two experiments were designed to capture the global performance throughout the reachable workspace and along an electrode insertion trajectory. For both types of experiments, trials were repeated ten times with the robotic system restarted each time to insure that errors in the homing procedure were also included in the evaluation.

A single workspace test involved isolated cyclic movement in each task space direction (p_x, p_y, ϕ), while the other two positions remained unchanged. Position repeatability is quantified as the RMS error from the average positions at each sample point in the tests. Task space accuracy is presented as the RMS error from the measured end effector position and the desired task space position. Table IV presents both the task space position repeatability and accuracy.

The performance of the robot along the electrode insertion path was quantified by following a single electrode insertion trajectory. Fig. 9 shows the insertion trajectory in a solid line,
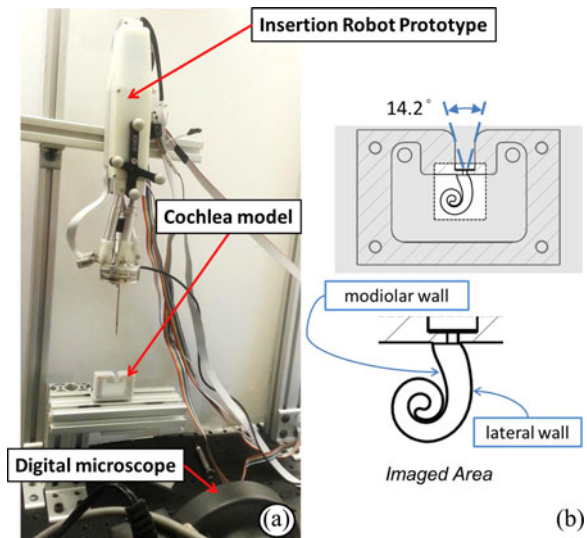

Fig. 10. Experimental Setup. (a) The insertion robot was mounted on a frame in lieu of a balance arm and registered to the cochleostomy in the phantom model. A digital microscope observed the insertion through the transparent front face of the phantom. (b) The model of the cochlea was provided by Cochlear Ltd. and adapted to a custom plastic holder. The access was designed to mimic the restrictions found in measured temporal bones. The center, nonshaded region represents the typical field of view for the digital microscope recording the insertion process.

target task-space error bounds of ±0.4 mm in dashed lines, the error bars for 20 discrete points sampled along the trajectory, and a greyed area showing the uncertainty stemming from the optical tracker error as provided by the manufacturer specifications. The figure shows that the accuracy along the insertion trajectory is better than the global accuracy throughout the entire workspace.

VIII. EXPERIMENTAL EVALUATION

To validate our system, several insertion experiments into a plastic cochlea phantom model were performed. This model was provided by Cochlear Ltd. and replicates the left-side temporal bone shape. To facilitate image acquisition, the cochlea model was removed from this phantom and a new mount was fabricated to allow use of a high-resolution digital microscope to record the insertion process. The mastoidectomy and access through the facial recess are also of a typical size with the passage through the facial recess having dimensions of 4.8 mm by 2.1 mm with an angular access of $\pm7°$. To prepare the model for realistic friction characteristics, the cochlea was filled with a 50% water/glycol solution. This lubrication choice has been presented in the literature [28] and validated against other types of lubrication in [36].

Fig. 10 shows the experimental setup prior to insertion including the robot, cochlea model, and digital microscope. For these experiments, the robot was mounted fixed relative to the temporal bone model and the gripper tip was manually registered to the cochleostomy through direct control from the user. A test electrode was loaded and the insertion platform moved to an initial position, bringing the tip of the PEA to the cochleostomy. The path planning was updated for the current electrode shape with a minimum depth of insertion before initiation of AoS to
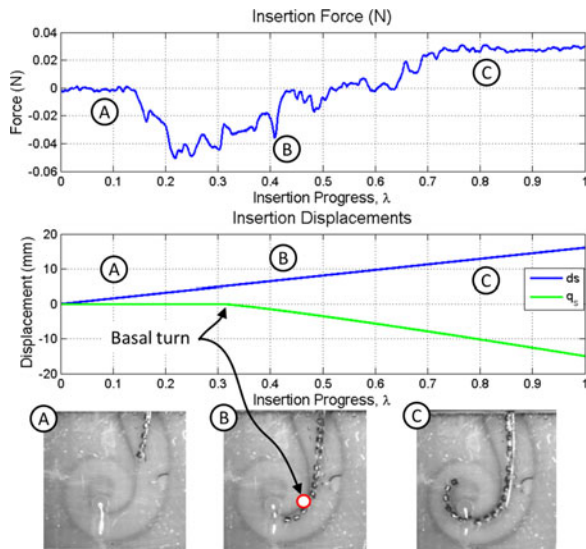
Fig. 11. Plastic model insertion results. The top plot presents the recorded insertion force data throughout the insertion process. The middle plot shows the robot trajectory planner's desired insertion depth and stylet actuation. Following the protocol of the AoS technique, the stylet is retracted at the same rate as the PEA advances. Photos of the insertion are labeled A, B, and C, and correspond to the similarly marked points on the middle plot. The basilar turn, the point where AoS begins, has been marked.
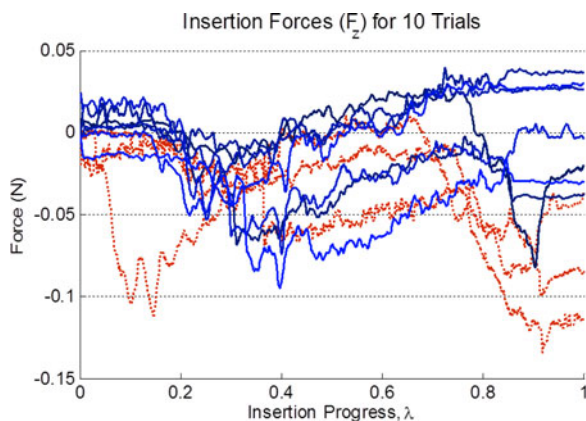

Fig. 12. Collective insertion force results in insertion direction for ten trials. Insertions at 0.3 mm/s are shown as dashed lines and insertions at 1 mm/s as solid lines.

be 5 mm. This series of insertions were set at a fixed linear insertion rates of 0.3 and 1 mm/s.

A. Experimental Results

A total of ten insertions on the phantom model were performed to quantify the magnitude of the insertion force. Fig. 11 shows a detailed look at one insertion with the force, displacement, and imaged PEA position. Electrode displacement, actuation, and forces are taken from the robot's real-time controller which records all data during the insertion process at a rate of 1 kHz. A review of insertion forces experienced during all evaluation insertions is shown in Fig. 12. Forces were kept below 0.08 N throughout the insertions while consistently maintaining forces below 0.04 N before the basal turn. This is consistent

with measured forces in [21] and [28]. It should be noted however, that in those prior studies, single axis components of force were presented while this system's measurements include all six components of the force and moment applied on the tool. Forces acting normal to the robot's plane of motion are called out of plane forces and varied up to 0.2 N in one case. The out of plane forces occur due to the registration error and exist in the null space of this tool's workspace. Lateral insertion forces (acting along $\hat{y}_b$ in Fig. 3) are of the order of 40 mN and may have the potential for further reduction through hybrid force control algorithms. The case of high out of the plane force did not have a noticeable impact on the insertion force. These forces are likely applied at the cochleostomy and the sliding friction with a minimal contact area is negligible in the lubricated model.

IX. Conclusion

This study presented the design of a new robot for CI insertion with the ultimate goal of mitigating trauma and providing reliable measurement of applied forces on the cochlea throughout insertion. The unique contributions of this design lie first in its compactness and ability to be deployed without altering the current clinical workflow for this procedure. Second, the wire-driven 3RPR parallel mechanism structure allows for designs that isolate motors from the surgical site and the solution to the decoupling of wire actuation to end effector position and orientation was presented. Calibration of the tool's kinematics used a method which considers the loading direction on the actuators without identifying explicit stiffness and friction parameters. Our continued efforts in the development of this device focus on improving the mechanical design, miniaturization, developing mechanism stiffness models, and more sophisticated algorithms for electrode placement and insertion fault identification.

References

[1] "Cochlear implants," National Institute of Health, Bethesda, MD, USA, Tech. Rep. NIH Pub. 11-4798, 2011.

[2] S. B. Waltzman and J. T. J. Roland, *Cochlear Implants*, 2nd ed. New York, NY, USA: Thieme Medical Publishers, 2006.

[3] M. Cosetti and J. T. Roland Jr., "Cochlear implant electrode insertion," *Oper. Techn. Otolaryngol., Head Neck Surg.*, vol. 21, no. 4, pp. 223–232, Dec. 2010.

[4] N. L. Cohen, J. T. Roland, and A. Fishman, "Surgical technique for the nucleus contour cochlear implant," *Ear Hear.*, vol. 23, no. 1, pp. 59S–66S, Feb. 2002

[5] A. Eshraghi, N. Yang, and T. Balkany, "Comparative study of cochlear damage with three perimodiolar electrode designs," *Laryngeoscope*, vol. 113, pp. 415–419, 2003.

[6] O. Adunka, W. Gstoettner, M. Hambek, M. H. Unkelbach, A. Radeloff, and J. Kiefer, "Preservation of basal inner ear structures in cochlear implantation," *J. Oto-Rhino-Laryngol.*, vol. 66, no. 6, pp. 306–12, Jan. 2004.

[7] B. M. Verbist, L. Ferrarini, J. J. Briaire, A. Zarowski, F. Admiraal-Behloul, H. Olofsen, J. H. C. Reiber, and J. H. M. Frijns, "Anatomic considerations of cochlear morphology and its implications for insertion trauma in cochlear implant surgery," *Otol. Neurotol.*, vol. 30, no. 4, pp. 471–477, Jun. 2009.

[8] H. N. Ibrahim, S. Helbig, D. Bossard, and E. Truy, "Surgical trauma after sequential insertion of intracochlear catheters and electrode arrays (a histologic study)," *Otol. Neurotol.*, vol. 32, no. 9, pp. 1448–1454, Dec. 2011.

[9] M. L. Carlson, C. L. W. Driscoll, R. H. Gifford, G. J. Service, N. M. Tombers, B. J. Hughes-Borst, B. A. Neff, and C. W. Beatty, "Implications of minimizing trauma during conventional cochlear implantation," *Otol. Neurotol.*, vol. 32, no. 6, pp. 962–968, Aug. 2011.

[10] H. H. King, R. Donlin, and B. Hannaford, "Perceptual thresholds for single versus multi-finger haptic interaction," in *Proc. IEEE Haptics Symp.*, Mar. 2010, pp. 95–99.

[11] G. Baud-bovy and E. Gatti, "Hand-held object force direction identification," *Lecture Notes Comput. Sci.*, vol. 6192, pp. 231–236, 2010.

[12] J. Zhang, K. Xu, N. Simaan, and S. Manolidis, "A pilot study of robot-assisted cochlear implant surgery using steerable electrode arrays," in *Proc. Med. Image Comput. Comput. Assist. Interv.*, Jan. 2006, vol. 9, pp. 33–40.

[13] J. Zhang, "Model and parameter identification of friction during robotic insertion of cochlear-implant electrode arrays," in *Proc. IEEE Int. Conf. Robot. Autom.*, May 2009, pp. 3859–3864.

[14] J. Zhang, "Inroads toward robot-assisted cochlear implant surgery using steerable electrode arrays," *Otol. Neurotol.*, vol. 31, no. 8, pp. 1199–1206, Jun. 2010.

[15] H. Lim, J.-M. Han, J. Hong, B.-J. Yi, S. H. Lee, J. H. Jeong, N. Matsumoto, M. Oka, S. Komune, and M. Hashizume, "Image-guided robotic mastoidectomy using human-robot collaboration control," in *Proc. IEEE Int. Conf. Mechatronics Autom.*, Aug. 2011, pp. 549–554.

[16] T. Klenzner, C. C. Ngan, F. B. Knapp, H. Knoop, J. Kromeier, A. Aschendorff, E. Papastathopoulos, J. Raczkowsky, H. Wörn, and J. Schipper, "New strategies for high precision surgery of the temporal bone using a robotic approach for cochlear implantation," *Eur. Arch. Oto-Rhino-Laryngol.*, vol. 266, no. 7, pp. 955–960, Jul. 2009.

[17] A. Reid, "A surgical robot for cochleostomy," in *Proc. IEEE 29th Annu. Int. Conf. Eng. Med. Biol. Soc.*, 2007, pp. 1229–1232.

[18] C. J. Coulson, A. P. Reid, D. W. Proops, and P. N. Brett, "ENT challenges at the small scale," *Int. J. Med. Robot. Comput. Assist. Surg.*, vol. 3, no. 2, pp. 91–96, Jun. 2007.

[19] A. Hussong, T. S. Rau, T. Ortmaier, B. Heimann, T. Lenarz, and O. Majdani, "An automated insertion tool for cochlear implants: Another step towards atraumatic cochlear implant surgery," *Int. J. Comput. Assist. Radiol. Surg.*, vol. 5, no. 2, pp. 163–171, Mar. 2010.

[20] D. Schurzig, R. F. Labadie, A. Hussong, T. S. Rau, and R. J. Webster, "A force sensing automated insertion tool for cochlear electrode implantation," in *Proc. IEEE Int. Conf. Robot. Autom.*, Anchorage, AK, USA, 2010, pp. 3674–3679.

[21] O. Majdani, D. Schurzig, A. Hussong, T. Rau, J. Wittkopf, T. Lenarz, and R. F. Labadie, "Force measurement of insertion of cochlear implant electrode arrays in vitro: Comparison of surgeon to automated insertion tool," *Acta oto-laryngologica*, vol. 130, no. 1, pp. 31–36, Jan. 2010.

[22] L. B. Kratchman, G. S. Blachon, T. J. Withrow, R. Balachandran, R. F. Labadie, and R. J. Webster, "Design of a bone-attached parallel robot for percutaneous cochlear implantation," *IEEE Trans. Biomed. Eng.*, vol. 58, no. 10, pp. 2904–10, Oct. 2011.

[23] M. Miroir, Y. Nguyen, G. Kazmitcheff, E. Ferrary, O. Sterkers, and A. B. Grayeli, "Friction force measurement during cochlear implant insertion: Application to a force-controlled insertion tool design," *Otol. Neurotol.*, vol. 33, no. 6, pp. 1092–1100, Aug. 2012.

[24] R. F. Labadie, R. Balachandran, J. E. Mitchell, J. H. Noble, O. Majdani, D. S. Haynes, M. L. Bennett, B. M. Dawant, and J. M. Fitzpatrick, "Clinical validation study of percutaneous cochlear access using patient-customized microstereotactic frames," *Otol. Neurotol.*, vol. 31, no. 1, pp. 94–99, Jan. 2010.

[25] C. B. Teszler, D. Ruimi, E. Bar-Meir, and M. Luntz, "Width of the extended facial recess: A numerical study of ultrahigh-resolution computed tomography and its implications in minimally invasive otologic surgery," *Otol. Neurotol.*, vol. 26, no. 4, pp. 782–789, Jul. 2005.

[26] J. Pile, M. Y. Cheung, J. Zhang, and N. Simaan, "Algorithms and design considerations for robot assisted insertion of perimodiolar electrode arrays," in *Proc. IEEE Int. Conf. Robot. Autom.*, Shanghai, China, 2011, pp. 2898–2904.

[27] G. Kontorinis, T. Lenarz, T. Stöver, and G. Paasche, "Impact of the insertion speed of cochlear implant electrodes on the insertion forces," *Otol. Neurotol.*, vol. 32, no. 4, pp. 565–570, Jun. 2011.

[28] J. T. Roland, "A model for cochlear implant electrode insertion and force evaluation: Results with a new electrode design and insertion technique," *Laryngoscope*, vol. 115, no. 8, pp. 1325–1339, Aug. 2005.

[29] C. B. Barber *et al.*, "The Quickhull algorithm for convex hulls," *ACM Trans. Math. Softw.*, vol. 22, no. 4, pp. 469–483, Dec. 1996.

[30] L. T. Cohen *et al.*, "Improved and simplified methods for specifying positions of the electrode bands of a cochlear implant array," *Amer. J. Otol.*, vol. 17, no. 6, pp. 859–865, Nov. 1996.

[31] B. M. Verbist *et al.*, "Consensus panel on a cochlear coordinate system applicable in histologic, physiologic, and radiologic studies of the human cochlea," *Otol. Neurotol.*, vol. 31, no. 5, pp. 722–730, Jul. 2010.

[32] N. Sima'an *et al.*, "Design considerations of new six degrees-of-freedom parallel robots," in *Proc. IEEE Int. Conf. Robot. Autom.*, vol. 2, Leuven, Belgium, May 1998, pp. 1327–1333.

[33] W. Townsend and J. Salisbury, "The effect of coulomb friction and stiction on force control," in *Proc. IEEE Int. Conf. Robot. Autom.*, 1987, vol. 4, pp. 883–889.

[34] L.-W. Tsai, *Robot Analysis: The Mechanics of Serial and Parallel Manipulators*. New York, NY, USA: Wiley, 1999.

[35] P. Chiacchio *et al.*, "Global task space manipulability ellipsoids for multiple-arm systems," *IEEE Trans. Robot. Autom.*, vol. 7, no. 5, pp. 678–685, Oct. 1991.

[36] G. Kontorinis *et al.*, "The effect of different lubricants on cochlear implant electrode insertion forces," *Otol. Neurotol.*, vol. 32, no. 7, pp. 1050–1056, Sep. 2011.

Jason Pile (S'10) received the Bachelor's degree in mechanical engineering from Northeastern University, Boston, MA, USA, in 2005, and the M.Sc. degree in mechanical engineering from Columbia University, New York, NY, USA, in 2010. He is currently working toward the Ph.D. degree in mechanical engineering at Vanderbilt University, Nashville, TN, USA.

From 2005 to 2009, he was an Assistant Staff Engineer at MIT Lincoln Laboratory.

Nabil Simaan (M'04) received the B.Sc., M.Sc., and Ph.D. degrees in mechanical engineering from the Technion—Israel Institute of Technology, Haifa, Israel, in 1996, 1999, and 2002, respectively.

During 2003, he was a Postdoctoral Research Scientist at The Johns Hopkins University National Science Foundation (NSF) Engineering Research Center for Computer-Integrated Surgical Systems and Technology, where he was engaged in research on minimally invasive robotic assistance in confined spaces. In 2005, he joined Columbia University, New York, NY, USA, as an Assistant Professor of mechanical engineering and the Director of the Advanced Robotics and Mechanisms Applications Laboratory. He has been an Associate Professor at Vanderbilt University, Nashville, TN, USA, since the Fall semester of 2010.

Dr. Simaan received the NSF Career Award for young investigators to design new algorithms and robots for safe interaction with the anatomy in 2009.